# Chapter 6. Fabrication, Assembly and Experimental Test Set-up

In the preceding chapters we have proposed several XY flexure mechanism designs, and also a performance analysis for each. Of all the designs considered, Design 6 is chosen for fabrication and testing because of its large range of motion, low cross-axes coupling errors, small parasitic yaw rotation of the motion stage, good actuator isolation and thermal insensitivity. The only drawback in this design is the variation in its inline axial stiffness over the range of motion, which is important while designing the motion system for a high bandwidth.

The objective of this experimental test set-up is to validate the analytical predications of the previous chapters. For the particular design being considered, we would like to measure the static, dynamic and thermal performance. Range of motion, primary stiffness, cross-axes coupling, actuator isolation, parasitic yaw error, change in inline stiffness are some of the static parameters of interest. Analysis and testing to determine the dynamic behavior and thermal response are part of the future work planned. Although the hardware and testing system has been designed to be able to allow all these tests, at present only static performance tests have been performed.

## 6.1 Metrology Objectives

It is desirable to measure the following aspects of the XY flexure stage and compare it with the analytically predicted behavior

- Range of motion and primary stiffness in the X and Y directions
- Variation of primary stiffness in X direction with Y loads, and vice versa
- Y displacement of the motion stage in response to an X actuation force, and vice versa
- Y displacement of Intermediate Stage 1, and X displacement of Intermediate Stage 2 in response to X and Y forces
- Rotation of the motion stage in response to X and Y forces
- Rotation of intermediate stages in response to X and Y forces
- Variation of inline axial stiffness between stage 1 and motion stage in response to a primary Y displacement, and vice versa

## 6.2 Choice of Material

To minimize assembly and manufacturing errors, a monolithic design was an obvious decision. The choice of material and raw stock is a key step in the hardware design. It is desired to start with a plate that a) has very low internal stresses because once the flexures are cut on the plate, the internal stresses relieve by distorting the thin flexure structures, and b) is very flat so as to make sure that the subsequent machining processes and the metrology alignment have a good reference plane. A plate coming from the supplier will typically not have the desired level of flatness, and any machining done to achieve flatness will add internal stresses to the plate. Although annealing the plate eliminates the internal stresses, it significantly reduces the yield strength of the material resulting in extremely poor range of motion. Furthermore, any annealing after a machining step, so as to reduce the machining stresses, results in a loss of dimensional tolerances obtained by the machining. Thus, it is very difficult to balance the requirements of high strength, good dimensional accuracy and low internal stresses. Based on the application one has to live with some compromises.

For the purpose of our experiments, we have chosen AL6061–T651. Invar and super invar were other choices that were considered because of their low coefficient of thermal expansion (CTE). But the design is thermocentric and therefore CTE was not a critical factor. Furthermore, these two materials have poor Yield Strength to Young's Modulus ratios as compared to Aluminum. Beryllium Copper was another choice because of its excellent $S_y/E$ ratio, but was rejected due to fabricability reasons.

Several Aluminum alloys are available that provide low internal stresses, good strength and phase stability. Among the AL alloys, 2000, 6000 and 7000 are the only heat treatable series, where strength improvement can be achieved by precipitation hardening without any cold working, which adds significant amounts of internal stresses. AL 2024 and AL7075 are aircraft alloys that offer very high strengths, whereas AL 6061 is common for regular use and has a moderate strength. AL 2024 T851, is strong and stable but has some amount of cold work done on it. AL 6061 T651 has intermediate strength, stable and very low internal stresses. Temper T6 corresponds to the highest strength level achieved only by precipitation hardening. The suffix –51 implies that plate stress are relieved by stretching the plate after it has gone through the rolling mill. Temper T6 is not recommended for AL 7075 because it is prone to fatigue corrosion. Instead tempers T7351 and T7651 are recommended. The literature recommends AL 6061 and AL 7075 for precision instruments due to their phase stability of long periods of time [87]. Ultimately, AL6061-T651 was selected because of its ease of availability, and good overall properties.

For our application we choose Kaiser plates, which are usually considered to have better dimensional tolerances. Flatness is quoted for 0.001inch per 1 inch, which is usually interpreted as follows – if an N inch long plate is placed on a flat table, then a shim of thickness 0.001N can be slid between the plate and

the table. The flatness of a 18 inch x 18 inch plate was actually measured on the Coordinate Measuring Machine (CMM), and was found to be flat within approximately 0.005 inch. Blanchard grinding or high speed machining may improve the surface flatness without introducing significant stresses. Also, the amount of machining required to make the above measured plate flat within 0.001 inch, which is desirable for the purpose of obtaining good reference surfaces, is not very significant.

### 6.3 Choice of manufacturing process

Two methods of cutting the flexure features on the above selected AL plate were considered and implemented: water-jet cutting (WJC) and wire electric discharge machining (EDM). Both these processes add minimal machining stresses to the part.

Wire EDM has traditionally been the machining method of choice for fabricating precision flexure mechanisms. Dimensional tolerances better than 0.0005 inch or 12 microns are easily achievable, and parallelism and perpendicularity of the machined feature can be tightly controlled. Also, with wire EDM the thickness of the plate being machined is not a concern, and uniform thickness flexure blades may be produced. But the process requires a fairly significant amount of set-up and is generally expensive.

The other machining option that has not been used much in the past is water-jet cutting. Several test cuts were made on an OMAX[1] water-jet cutting machine, to assess its machining capabilities because no such studies are available in the literature. The machine uses a mini-jet nozzle with an orifice size of .010 inch and operates at a pressure of 40,000 psi. The conclusions derived from these tests are presented here.

1. The true positioning accuracy of the machine axes is of the order of 0.001- 0.002 inch. Accuracy of the resulting part and features also depends critically on how well the plate is fixtured to the machine-bed. Part shift is a common source of dimensional variations. Straightness of cut has been measured to be within 0.001 inch over 15 inches. Cuts are flared close to the ends because the nozzle has to slow down as it approaches ends and corners. Therefore longer cuts are straighter. Parallelism of 0.001 inch over 15 inches, and perpendicularity of 0.004 inch over 15 inches was measured.
2. One of the biggest drawbacks of waterjet cutting is that it does not produce straight walls. The walls are not only tapered, but the taper varies with the location of the cut. During long straight cuts, kerf width is larger on the top as compared to the bottom, because the abrasive loses momentum as it reaches the bottom. On the other hand, when the nozzle is cutting close to a corner, a different phenomenon dominates the quality of cut. Since there is a lag between the top and bottom in the

[1] Trademark of OMAX Corporation

cutting frontier, corners tend to get rounded at the bottom. Obviously, this lag, illustrated in Fig 6.1a, increases as the nozzle speed increases. To minimize this, the machine slows down so that this lag is reduced to some extent. Nevertheless, corner radii are larger at bottom as compared to the top. Also, the slowing down of the nozzle increases the material wear and therefore the kerf width at the bottom. Thus, if a blade is cut on the waterjet machine, its resulting geometry is as illustrated in Fig. 6.1b.

The wall taper depends on many factors including the nozzle wear, abrasive grit size, the material being cut, water-pressure speed of the nozzle, and is hard to predict in a deterministic fashion. The most critical of these factors is the quality of the nozzle which includes a jewel, to create the water jet, and a mixing tube, to mix the abrasive and high pressure water. If the two have worn down, the jet is flared and the above effects become very prominent. With a brand new nozzle, and with a fine grit abrasive, tapers of less than 0.001inch over 1 inch were measured. For worn down nozzles, this number was as large as 0.008inch over 1 inch.

The XY flexure mechanism was eventually fabricated using both methods, to allow for a comparison between the two manufacturing options. All alignment features that shall be used in metrology should be machined in the same set-up as the rest of the flexure blades. This is important to ensure that the metrology axes are aligned well with the flexure axis. This significance of this alignment is described in Section 6.7.

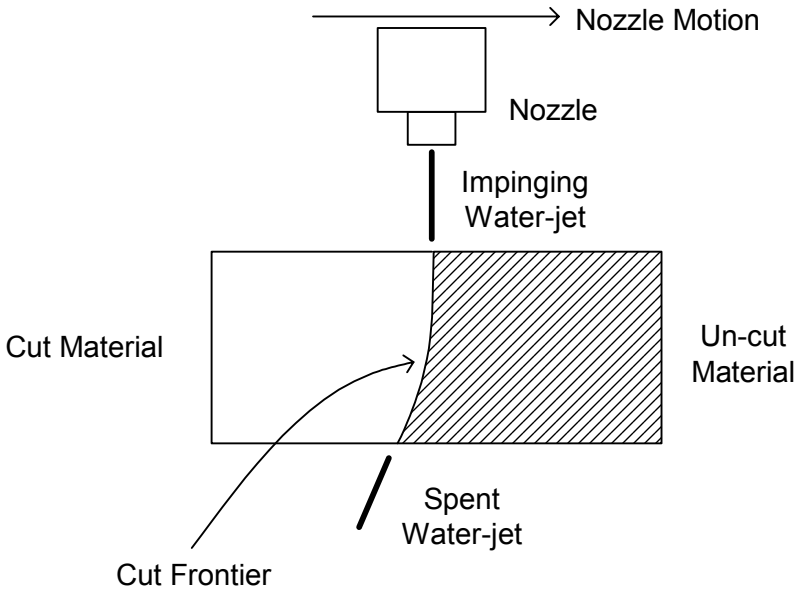


*Fig. 6.1a Cut frontier shape and lag between top and bottom in water-jet cutting*

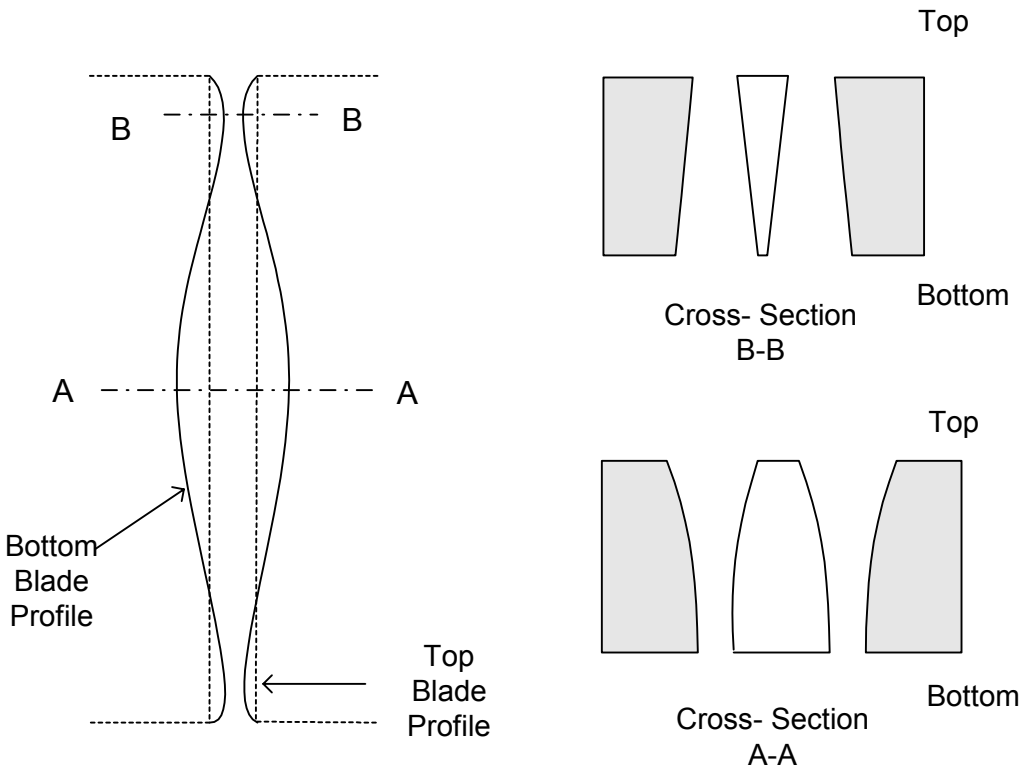


*Fig. 6.1b Exaggerated geometry of a blade cut by a waterjet machining*

The design of the experimental set-up includes the choice of sensors and actuators and their integration with the flexure mechanism. The experimental set-up used in this case has been designed such that it may be tested using multiple sensors and actuators. Also, the assembly is modular so that various different flexure mechanism designs can be tested using the same set-up. Particular care has been placed in 'designing in' alignment features for the actuator and sensors. Also, it has been ensured that the assembly has no interfaces that may introduce friction or backlash. All connections are designed to be friction based and the use of set-screws has been eliminated.

## 6.4 Actuation Methods

Selection of actuators that provide the desired range of motion and that too accurately is a tough challenge. Most voice coil or similar electromagnetic actuators that provide a direct force source become bulkier with the increased force requirements associated with large ranges of motion. Electromagnetic actuators, for example DC or stepper motors, with a gear-head and/or micrometer do not have the resolution necessary for nano-positioning. These actuators allow for a large range of motion and are

generally suitable for micro-positioning. Piezoelectric actuators are excellent in terms of quality of motion and the force generated, but provide very small ranges of motion. It is common to use these in conjunction with motion amplifiers [35-36] to achieve larger ranges of motion. Issues associated with amplifiers, such as reduction in effective actuator stiffness and lost motion, are discussed in much detail in the literature [6]. Piezo based inch-worm actuators are another choice for large range motions but have limited resolution.

To achieve both large range and high resolution, we decide to use a coarse-fine actuation scheme. The coarse actuator selected for this application is a PhysikInstrumente (M-227.25) DC mike actuator. This actuator is powered by a 2Watt Faulhaber DC motor with a gearhead and an integrated optical encoder. The output of the gearhead is connected to a precision PI micrometer with a non-rotating tip feature. The sensor resolution is 3.5 nanometers, and a backlash of about 2 microns. By means of feedback control, unidirectional repeatability of about 0.25 microns has been achieved. This motion accuracy and repeatability is limited by the significant amount of friction present in the gearhead and micrometer. Furthermore, because of the micrometer drive, the actuator is isolated from the system that it actuates. The only affect of the system is in the form of a variation in the friction depending upon the axial force. Several advanced techniques of motion control design in the presence of friction [89] were investigated to achieve better positioning capabilities, but were not successful. All these strategies are based on a somewhat deterministic model of friction that is expected to be repeatable. The friction present in this actuator was measured to be non-deterministic and non-repeatable. It was therefore decided to attain higher resolution by means of a piezo actuator attached to the tip of the coarse actuator.

The X and Y actuators are mounted in-plane on the flexure plate using a very simple yet effective clamping mechanism shown in Fig. 6.2. This mechanism ensures a well-distributed holding pressure over a length of the micrometer without damaging the lead-screw, and also a very well aligned axis of actuation. Further details on the clamping mechanism are presented in Section 6.6.

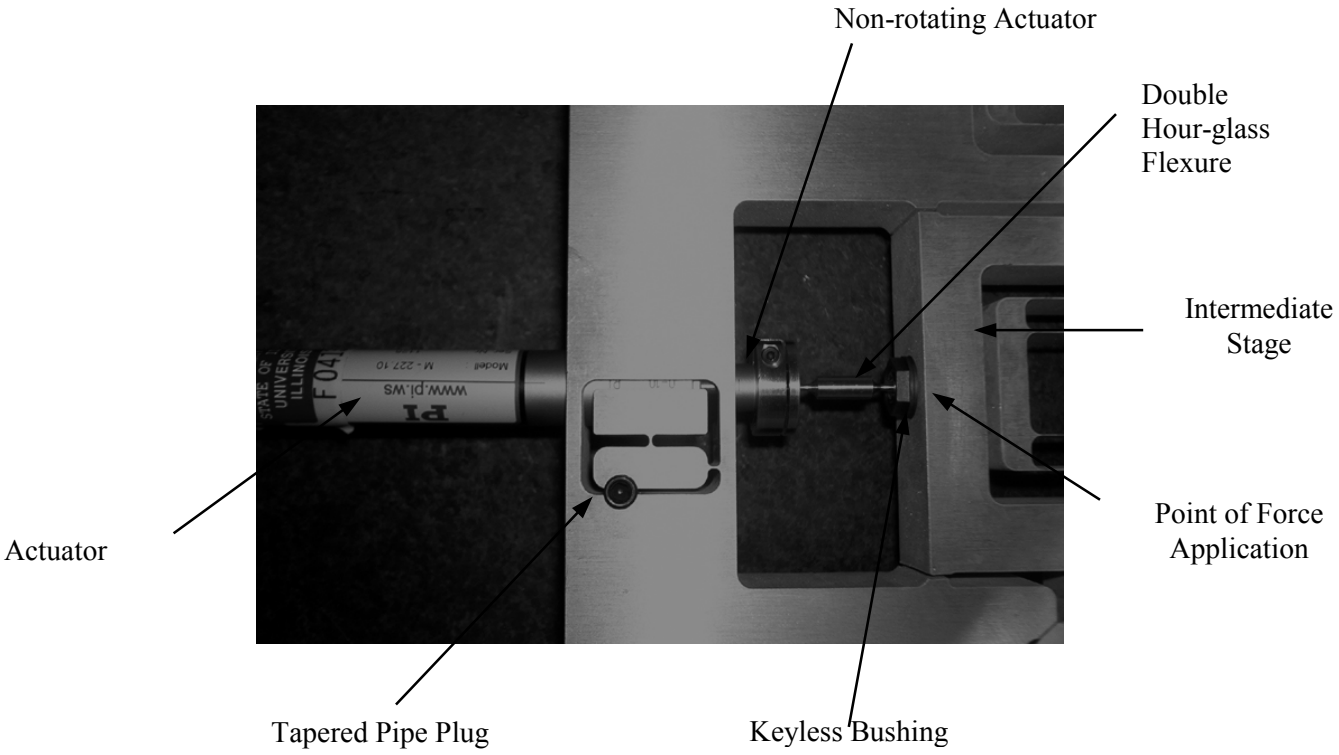


*Fig.6.2 Actuator Clamping Assembly*

Based on estimates of the transverse displacement and rotation of the intermediate stage a decoupler is needed between the actuator tip and the point of force application. This ensures that only an axial force is transmitted to the intermediate stage and any other loads arising due to misalignments are absorbed by the flexible coupling. A double hour-glass flexure, shown in Fig. 6.3a serves the purpose of this flexible coupling. One end of the double hourglass flexure is attached to the non-rotating cylindrical actuator tip by means of a friction clamp, while the other end is attached to the point of force application on the intermediate stage by means of a keyless bushing. Thus, throughout the actuation assembly all connections are based on friction clamping, and therefore free of backlash.

Furthermore, an piezoelectric stack that provides fine motion can be incorporated within the decoupler design, as shown in Fig. 6.3 b. The piezoelectric actuator used is from Queensgate Instruments and provides a 15 micron range of motion, and nanometric resolution.

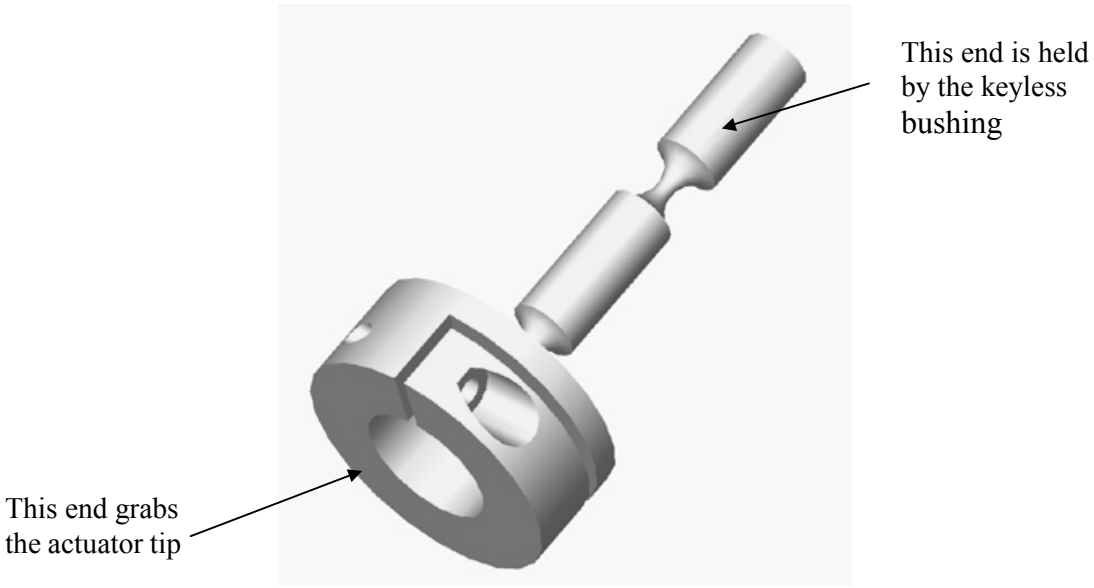


*Fig. 6.3 a) Passive decoupler design. B) Decoupler with an integrated fine actuator*

For the purpose of testing we also decided to use calibrated weights. This is a simple and inexpensive way of applying forces, as opposed to the previous actuators that are displacement sources. The same keyless bushing as earlier connects a support wheel to the intermediate stage. A fishing line can be threaded through one of several fine holes in the support wheel and is supported on a pulley on the other end. This allows us to apply additional moments to the intermediate stage, and test the mechanism for sensitivity against alignment errors arising from machining or assembly tolerances. The support wheel can be rotated $90^{o}$ to test the out of plane parasitic motion behavior of the mechanism. These ideas are illustrated in Figures 6.4a and b.

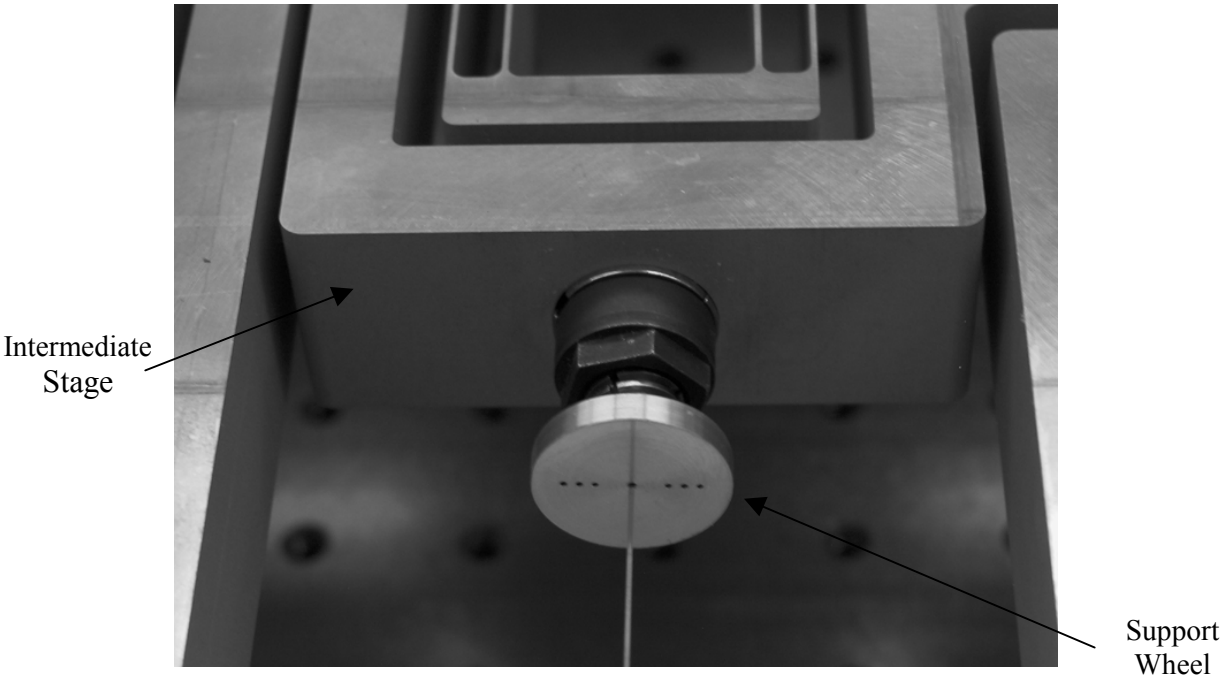


*Fig. 6.4a. Support wheel to transmit forces using a fishing line*

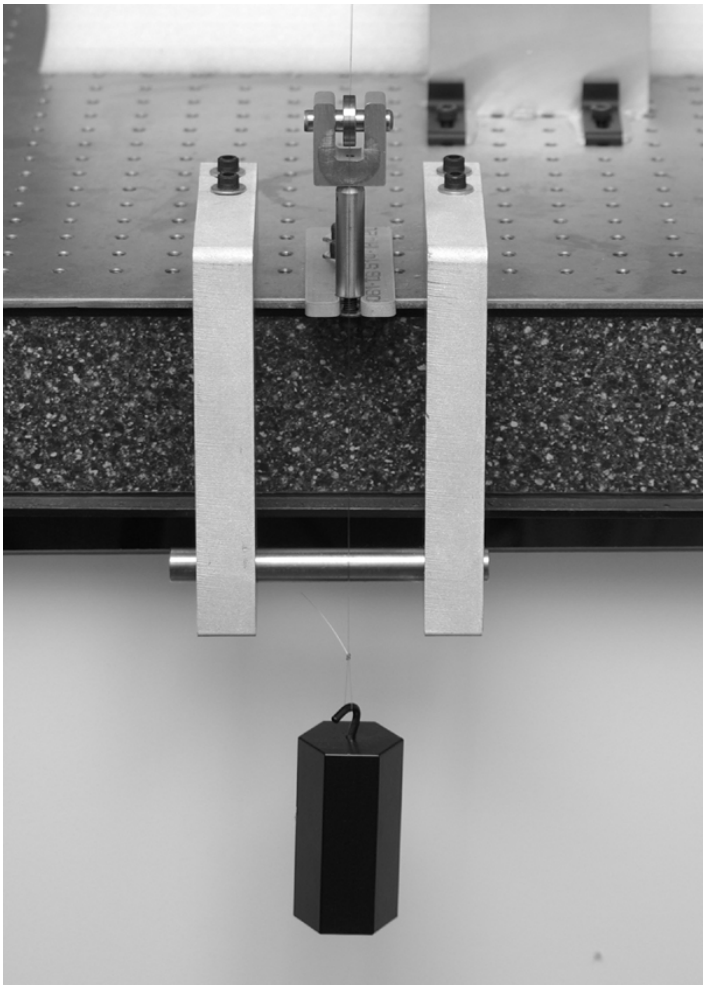

*Fig. 6.4b. Ball bearing based pulley to support the actuation weights*

The entire arrangement is very simple to assemble and disassemble, and the two actuation schemes based on force source and displacement source can be switched with relative ease. In the latter case, we notice that introduction of a ball bearing as the pulley, which becomes the source of non-deterministic effects that are observed in the measurements. A much better strategy to implement the above idea is by means of a virtual pulley as shown in Fig. 6.5, which eliminates the problems of friction, creep and hysteresis.

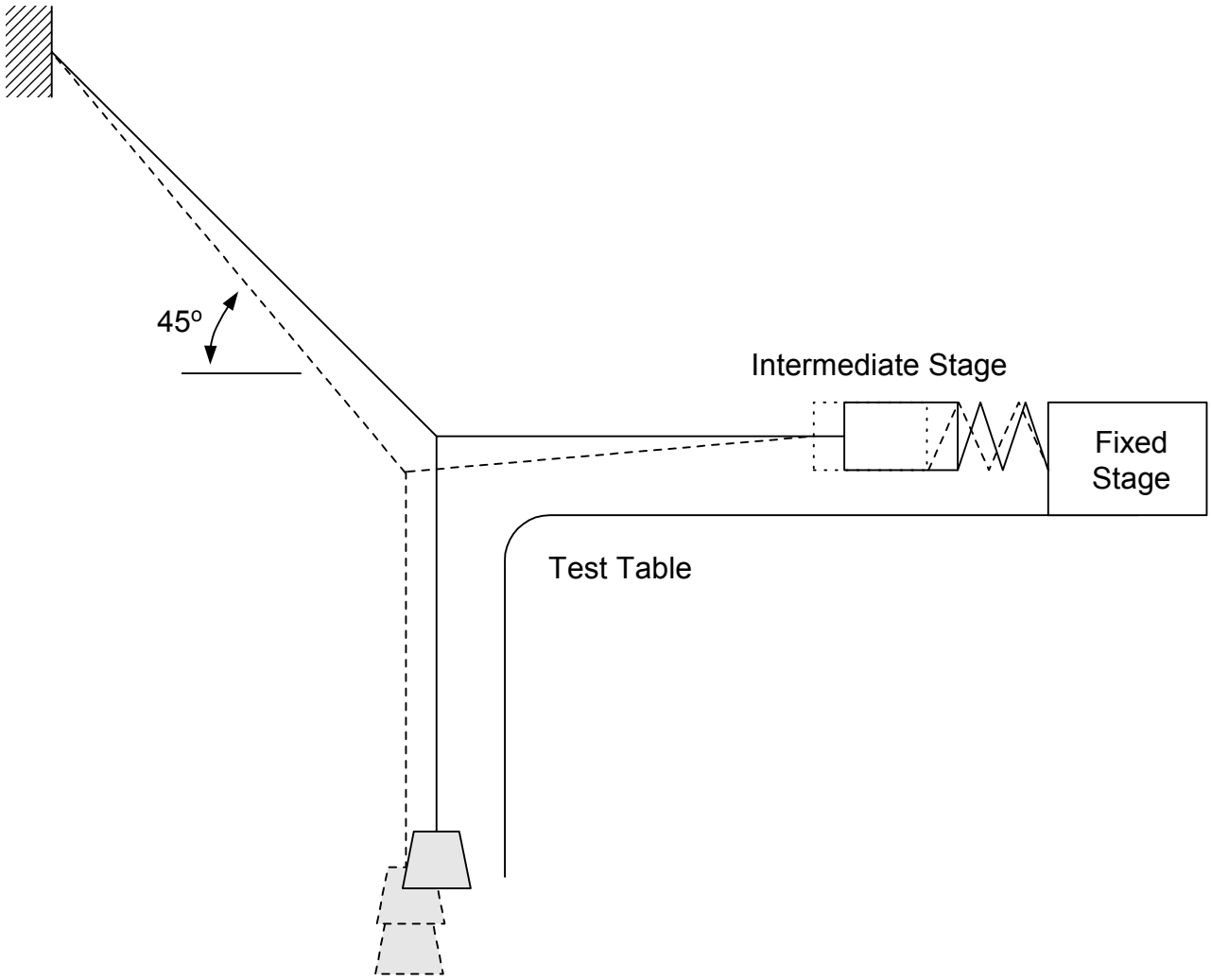


*Fig. 6.5 Concept of virtual Pulley*

## 6.5 Sensor Schemes

Multiple sensor schemes are incorporated in the experimental test design to maintain redundancy in measurement. This provides a check on the quality of data being measured.

As was discussed in Section 2.1, it is very difficult to obtain a sensor that has a high dynamic range, i.e., large range and small resolution. In fact both the sensor schemes that were used for testing, optical interferometry and capacitance sensing, are used only for the purpose of characterization, and cannot be used if the flexure mechanism were to be used for a motion control stage. Laser interferometry based

equipment is too bulky to be practical for regular use, and capacitance probes have a small dynamic range. High resolution two axis optical scales have become available only recently, and will be used in future measurements and motion stage design based on this flexure mechanism.

In both the sensing schemes, we mount a target block at the center of the motion stage, and it is the motion of this target block that is sensed by the transducers. The importance of the alignment between the flexure axes and the target block may be evident and is discussed in much detail in Section 6.6. One of the steps taken to ensure good alignment is that the holes for the three pins that position the target block with respect to the motion stage are machined during the same step as that for the flexure blades. Fig. 6.6 provides a close-up of the target block aligned and attached to the motion stage. The target block is a True Square from Starret, that is provides highly flat and orthogonal surfaces that are polished to mirror finish.

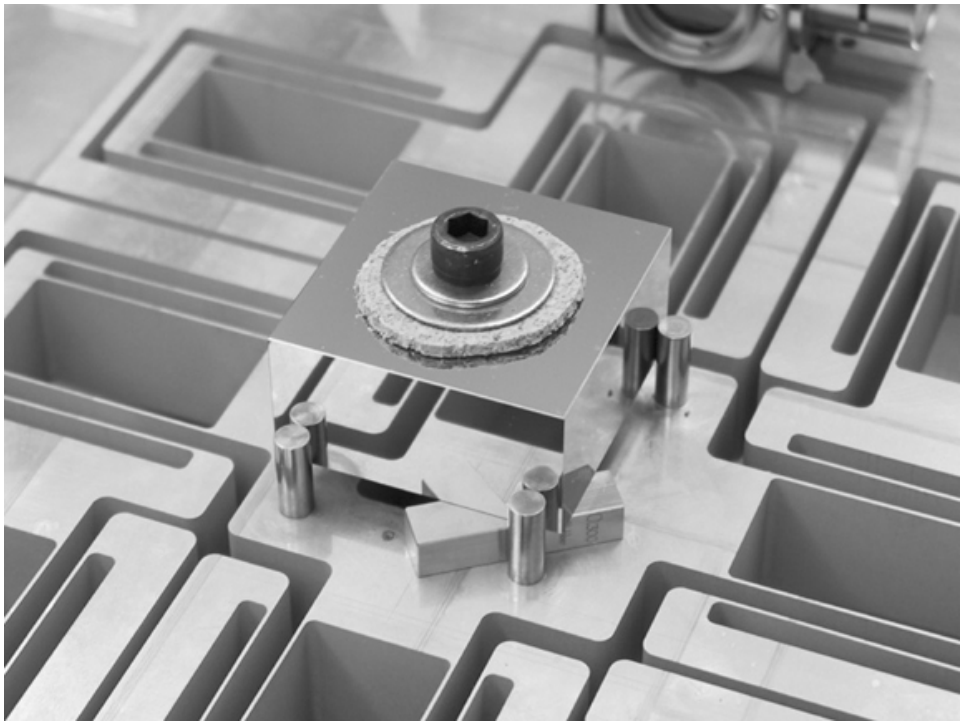

*Fig. 6.6 Metrology Target Block*

Fig. 6.7 presents a schematic of the optical metrology that is used to measure the displacements of the motion stage. A standard plane mirror interferometry arrangement is employed to measure the X and Y displacements of the motion stage. The interferometry equipment used is from HP/Agilent and provides a resolution of 5nm.

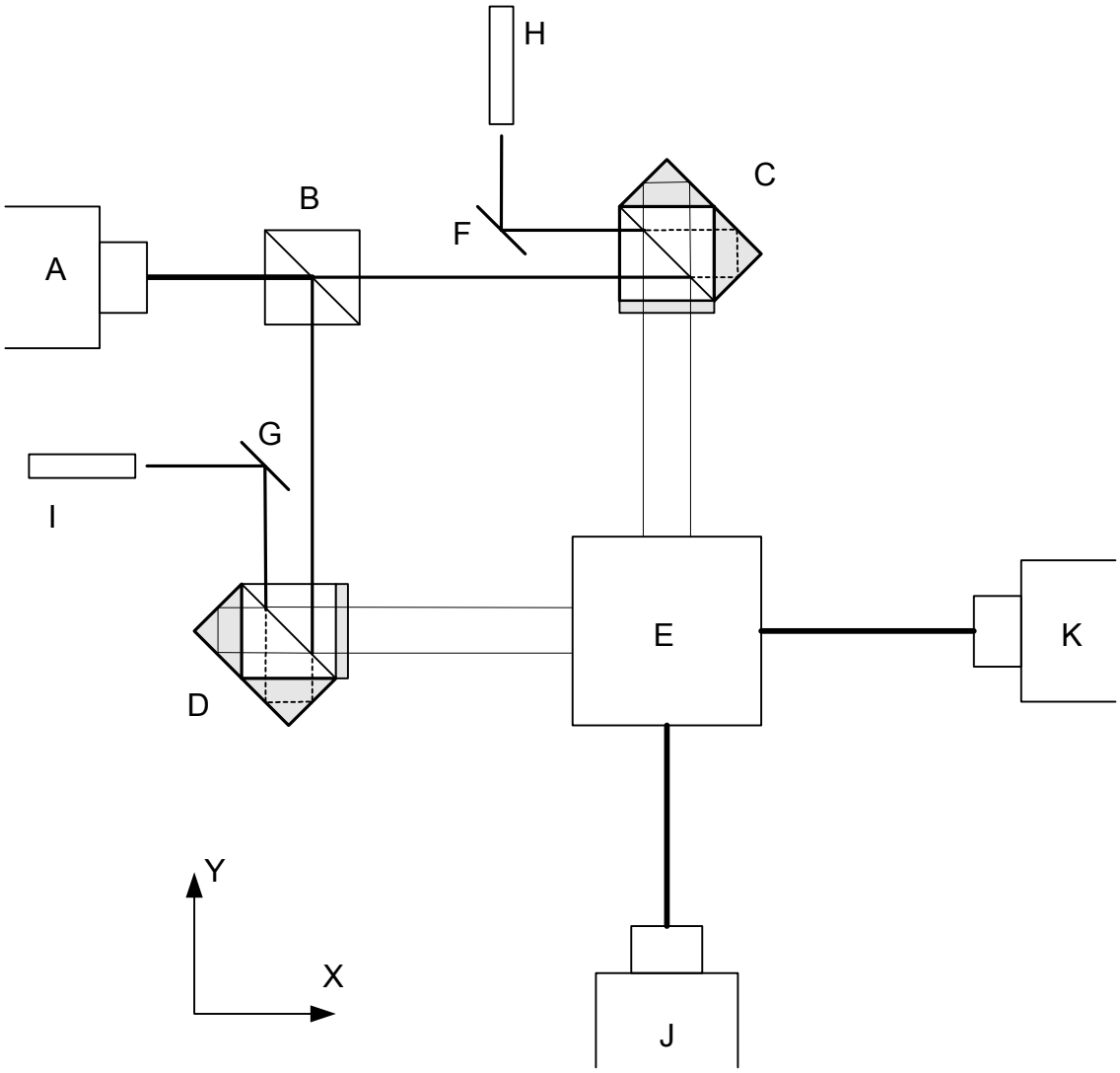


*Fig.6.7 Schematic of Optical metrology set-up*

In the above figure, A is the laser head, B is 50-50 beam splitter, C and D are plane mirror interferometers, E is the target block that moves with the motion stage, F and G are plane mirrors, and H and I are receivers that gather the two returning laser beams. Fig. 6.8 provides a picture of the above schematic during a measurement.

Apart from the plane mirror interferometry, two autocollimators are also used to simultaneously measure the motions stage rotations. J and K are dual axis autocollimators that measure $\theta_z$ and $\theta_x$, and $\theta_z$ and $\theta_y$ respectively. The angular resolution that can be obtained with these is 0.01 arc seconds.

Ideally it is desirable to take measurement from all these transducers during one single set-up, but that may not always be possible due to practical reasons.

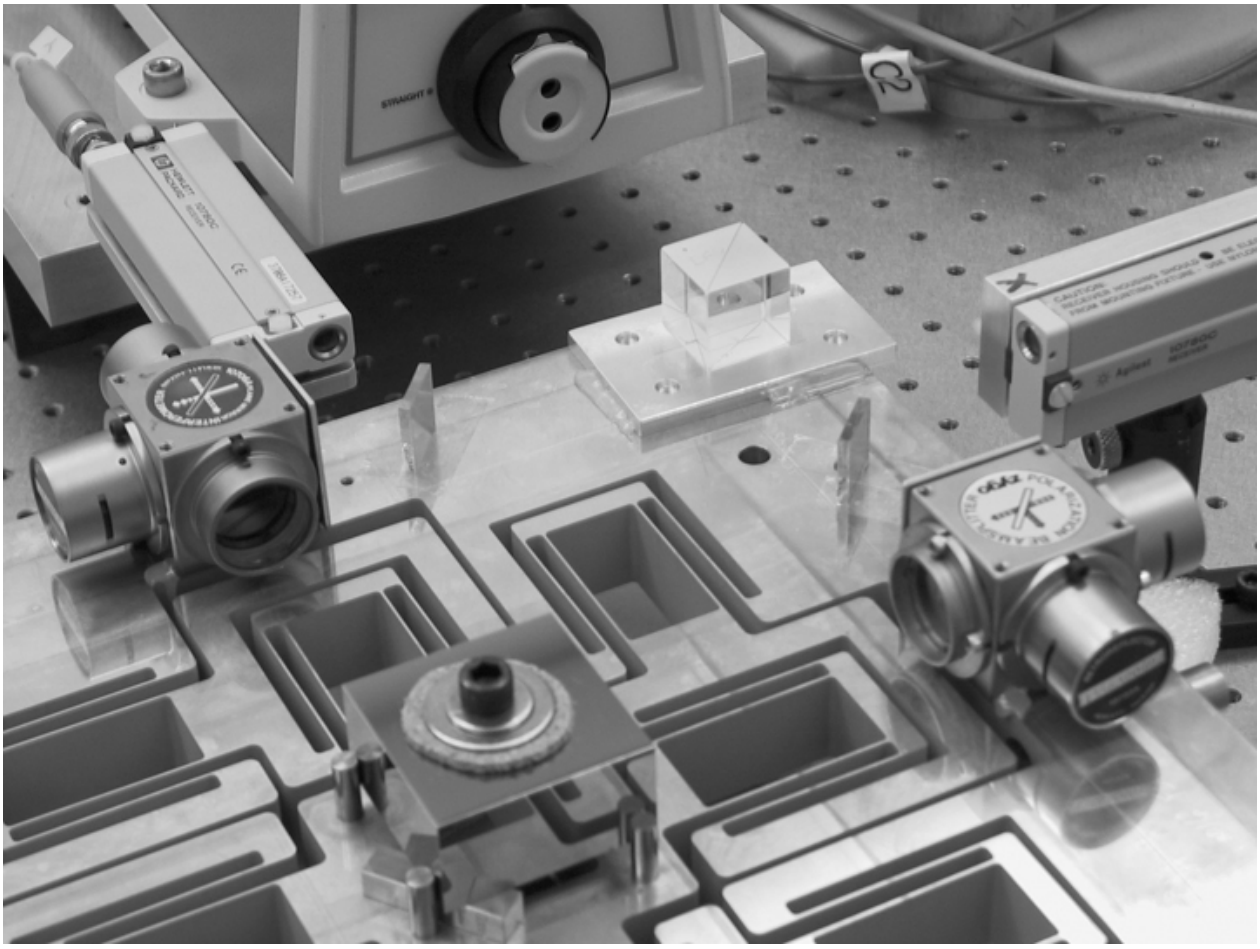


*Fig. 6.8 Plane mirror interferometry for X and Y displacement measurement*

The other set of sensors used are capacitance probes, which allow measurements over a 50 micron range and provide a resolution of 5nm. Cylindrical capacitance probes by Lion Precision Inc. have been used for this purpose. The capacitance probes are mounted on a metrology plate that surrounds the target block. The metrology plate is attached to the static periphery of the flexure mechanism and kinematically aligned with respect to the flexure axes by means by three pins. Spring are used to preload the three arms of the metrology plate against the pins. This may be evident in Fig 6.8, which shows an assembly which is set-up for capacitance probe based measurements.

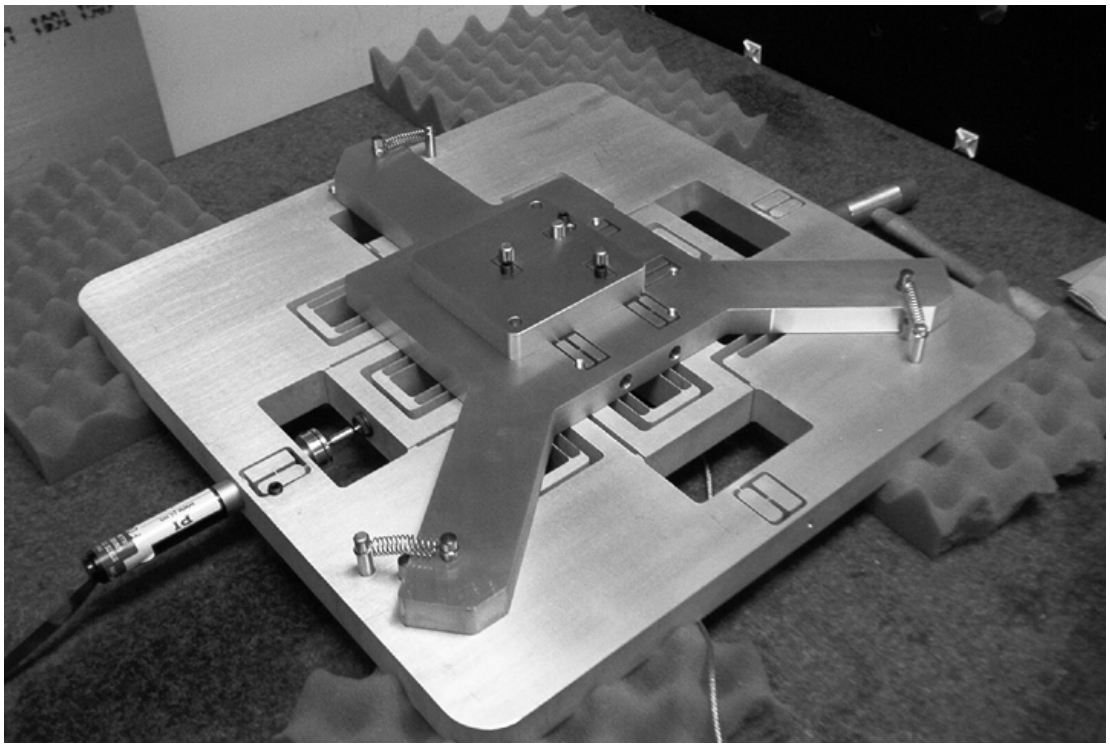

*Fig. 6.9 Capacitance probe based meteorology set-up*

The holes for the cap probes are drilled with reference to these machined surfaces that rest against the pins. Clamping mechanisms similar to that in Fig. 6.2 are used to hold the in-plane cap probes effectively in place. Another plate which holds three cap probes normal to the target block goes on top of the metrology plate. Thus, all six motions of the target block may be measured with the same sensor arrangement. This arrangement of cap probes, also referred to as the sensor nest, is shown in Fig. 6.10.

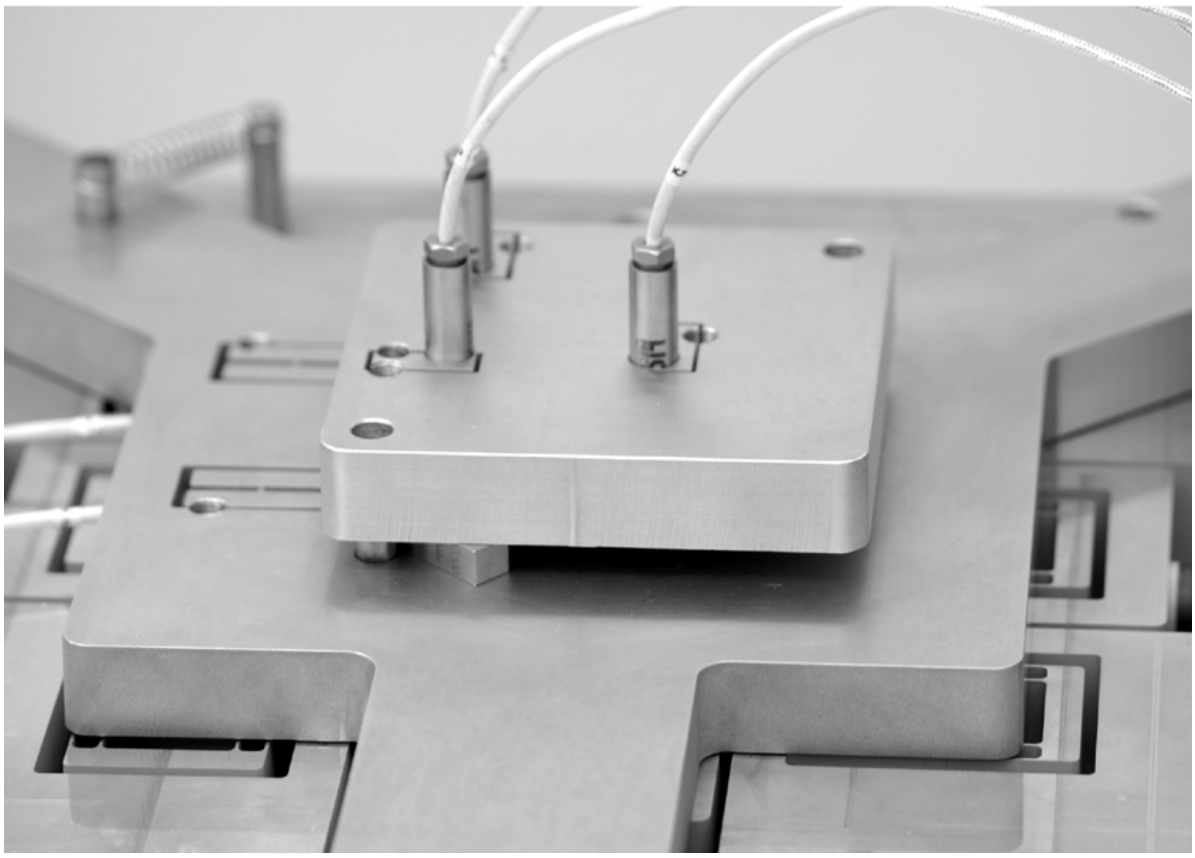

*Fig. 6.10 Capacitance sensor nest*

## 6.6 In-plane Capacitance Probe/Actuator Clamping Mechanism

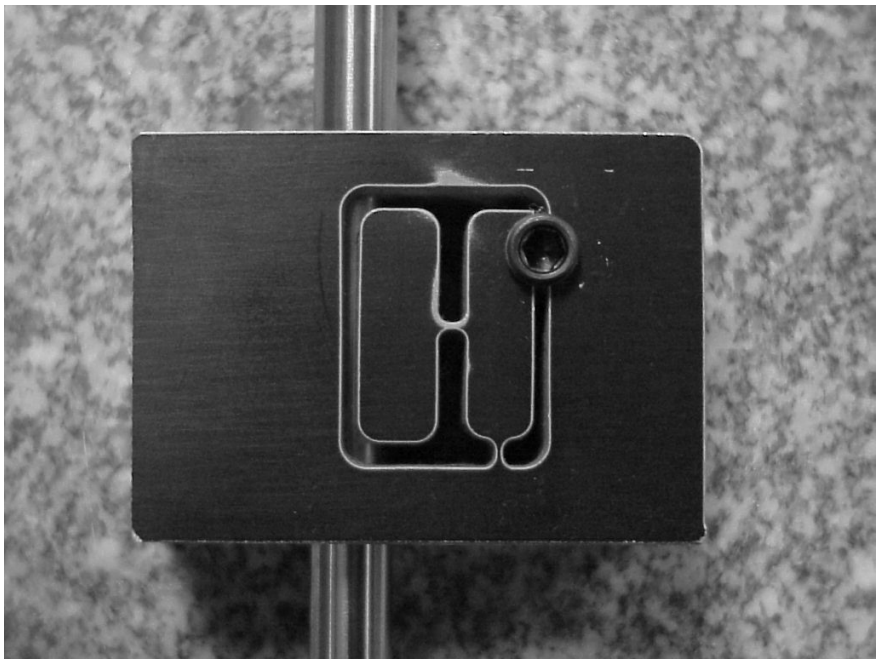

*Fig. 6.11 Clamping mechanism*

In our application, and in precision metrology in general, it is frequently required to hold capacitance probes such that they are properly aligned and held well. Alignment, i.e., parallelism between the sensor surface and the target surface, is important for measurement accuracy. Deviation from parallelism introduces cosine errors in the measurements. The sensor also needs to be held snugly in place by means of a well distributed nestling force. A loosely held cap probe is prone to mechanical as well as electrical noise. On the other hand, applying a large localized force, for example by means of a direct-contact set screw, can damage the cap probe and permanently alter its calibration. Furthermore, before the sensor is held in place, it must be free to move along the sensing axis to allow an adjustment of the initial gap between the sensor and the target. Thus, an ideal probe holding mechanism should enable the following:

1. Proper alignment
2. Nestling force distributed over a length of approximately two to three times the diameter of the probe
3. Easy movement of the probe along the sense axis before it is clamped

Similar concerns exist in actuator mounting as well.

While it is quite easy to hold a cylinder normal to plane, the same cannot be said about holding it in-plane for the simple reason that normal to plane cuts are far more feasible and inexpensive to make as compared to in-plane cuts, which may even be impossible as illustrated in Fig. 6.12.

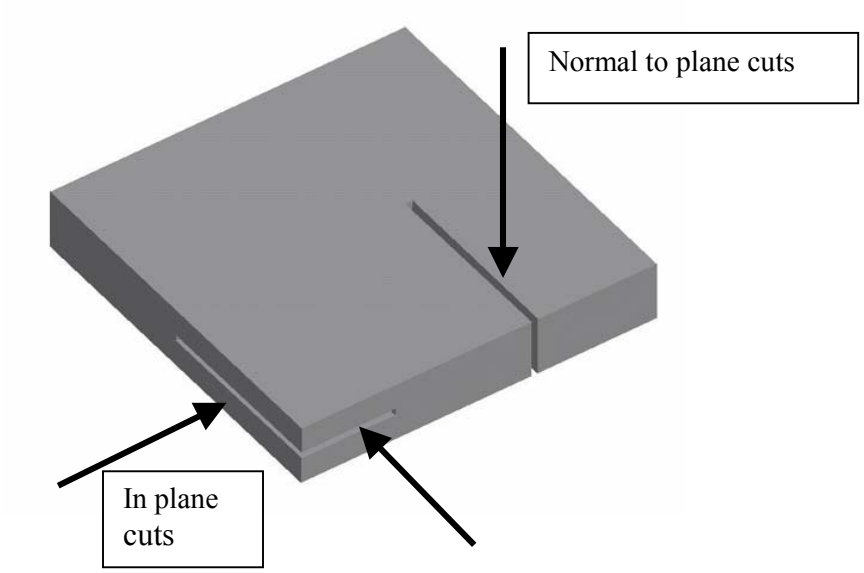


*Fig 6.12 In-pane and normal to plane cuts*

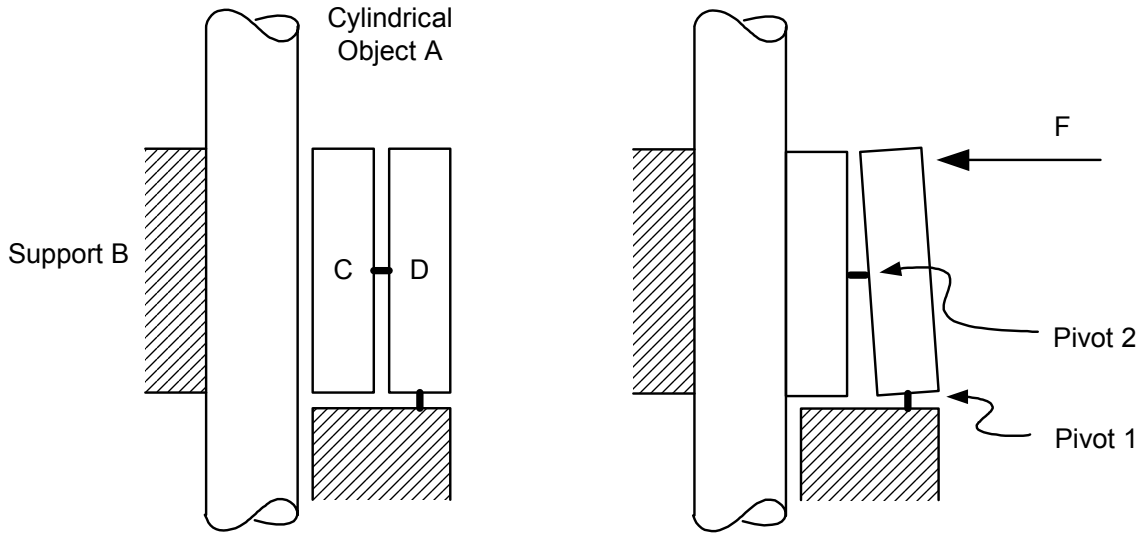


*Fig. 6.13 Proposed clamping mechanism*

In Fig. 6.13, we describe a very simple yet effective mechanism that we have employed to hold cap-probes and micrometers without damaging them. The arrangement consists of a cylindrical object A that is to be held firmly with respect to fixed support B. Furthermore, there are two blocks C and D connected by means of flexural pivot 2. Block D is connected to ground via the flexural pivot 1. Pivots 1 and 2 are designed such that they have a very high axial stiffness but low moment stiffness. Thus, flexural pivot 1 ensures that the force F that is applied on block D is not countered by any significant moment at Pivot 1 and is instead transmitted on to block C. Meanwhile, pivot 2 transmits this force to block C which nestles the object A against support B, without transmitting large moments. Pivot 2 allows a small relative rotation between blocks C and D without producing any significant enough moment on block C, since its moment stiffness is very small.

Thus ultimately, only a normal force acting at the middle gets transmitted to block C. This force distributes itself over the entire length of block C which secures part A against the fixed support B. The resulting pressure distribution at the interface of part A and block C is somewhat like a bell-curve, as is shown in a subsequent FEA study. Barring space constraints, it is very easy to increase the width of block C, which will result in a yet more uniform distribution of the applied force. This is guaranteed by St. Venant's Principle. The use of a single lever, i.e., block C without block D, supported by Pivot 1 would cause a stress concentration at the tip of the lever where it touches the cap probe, and potentially damage it. On the other hand, Pivot 2 in the proposed mechanism transmits only a normal force, and allows block C to align with Object A without producing any significant moment loads on Object A.

The in-plane nestling force can be applied very easily by means of an NPT tapered pipe plug, which is simply a set screw with tapered threads. While fabrication might seem to be a concern in this case, in reality it is quite straightforward as long as a particular order is followed. First the entire 2-D pattern can be cut using a waterjet machine or a wire EDM. This results in a part with blocks C and D supported merely by thin flexures. To drill the hole that will hold the object A, blocks C and D have to be temporarily held strongly in place. This is accomplished by gripping the part between two sheets of emery paper in a regular vice. As the vice jaws are tightened, the grit particles of the emery paper dig into the part including blocks C and D, and hold them firmly in place. Now the part can be drilled and reamed as though it were rigid. A spiral flute reamer is recommended since the cut is discontinuous. Once the part is drilled and reamed, either the object A or an artifact of the same diameter should be slid into the hole. With this is place, the hole for the tapered pipe plug can be tapped easily. Alternatively, one can leave supporting tabs while cutting the part initially on the waterjet / wire EDM. These supporting tabs keep the part stiff during subsequently machining. Once all the machining is done, these supporting tabs may be removed by using a very fine end mill cutter, or a fine saw blade, or even by a waterjet. Another way

would be to drill and ream the hole first, then align the part on a waterjet machine or wire EDM, and finally cut the 2-D pattern. Depending on the machine used this alignment may or may not be a straightforward step.

## 6.7 Metrology Alignments

In the error mapping of an XY stage, the primary objectives are to measure the cross-axis and yaw motion errors of the stage. There are several deviations from ideal behavior that can occur in this measurement. Some of these are attributed to the stage itself and other are attributed to the metrology set-up. We proceed to define various kinds of errors that are traditionally associated with serial stage design and metrology. In Fig. 6.14, X and Y represent the ideal system axes along which all components of the system would be aligned if the manufacturing and assembly were flawless.

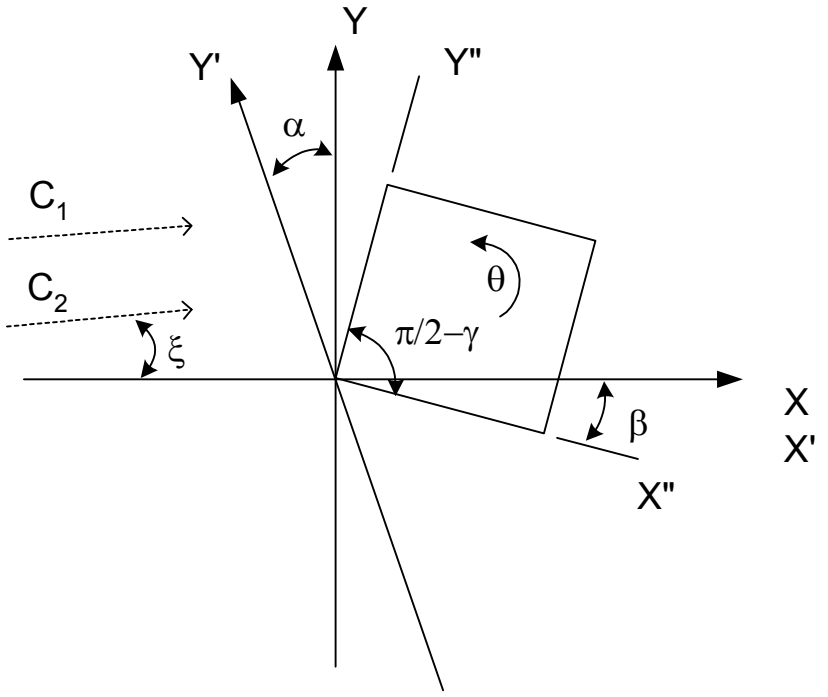


*Fig. 6.14*

Errors resulting from imperfect behavior of the stage are -

1) Orthogonality error: The actual axes of the stage, X′ and Y′, may not be perfectly orthogonal. For serial stages, this is typically due to an improper mounting and assembly of the bearing-ways. A motion along the Y′ results in a cosine error along the Y axis measurement and a sine error along the

X axis measurement. The deviation from orthogonality is quantified as the angle $\alpha$ in the above figure.

2) Straightness error: Straightness error shows up during a motion along Y′ as a non-linear variation in the X axis measurement, and results due to a non-ideal Y axis bearing-way. Since this error is not linear, it cannot be expressed in terms of an angle, and is therefore not shown in the above figure.
3) Yaw error: Yaw error is the actual yaw, $\theta$, of the motion stage as it moves within its range of motion

The above definitions are based on a serial arrangement of the X and Y bearing ways. For parallel stages, the idea remains similar, but the interpretations are slightly different. In this case, the orthogonality error and the straightness error are not two independent entities because they arise from the same kinematics or mechanics. The two together form the cross-axis error, which will have a linear component (corresponding to the orthogonality error), and a non-linear component (corresponding to the straightness error).

The metrology set-up invariably involves a set of sensors that are fixed to the ground and aligned with the ideal stage axes, an artefact attached to the motion stage that acts as the target for the sensors and is aligned with the stage axes. Irrespective of whether the stage is serial or parallel, the errors associated with metrology remain the same. These are,

1) Artefact geometry error: The artefact is usually such that it provides two very straight edges that are close to perpendicular.[2] The lack of orthogonality between the artefact axes X″ and Y″ is captured by the angle $\gamma$ in Fig. 6.14.

2) Artefact alignment error: This represents the misalignment between the artefact axes and the stage axes, for example the angle $\beta$ shown between X′ and X″ in the above figure. One usually employs precision ground pins pressed into precision drilled holes to achieve the best possible alignment. Nevertheless this misalignment remains, and results in a sine error in the X axis measurement when the stage moves along the Y′ axis.

3) Artefact straightness error: This relates to the lack of straightness of the artefact faces, and is not shown in the above figure. Typically artefact straightness is several orders of magnitude better than the stage straightness error itself and is therefore not an important contributor.

4) Sensor alignment error: This is the angle that the sensor line of measurement makes with the ideal system axes. This is the typical cosine error, represented by $\xi$, which can be minimized by careful alignment of the sensor axes.

[2] Manufacturing a straight-edge is much easier than producing two perfectly orthogonal edges.

While the importance of careful metrology set-up is unquestionable, it is an objective of the metrologist to design the experiment to be insensitive to the metrology set-up errors, and be the most responsive to the stage errors. By making multiple in-plane measurements and employing principles of reversal, one can cleverly discard some of the metrology related errors. Some examples are presented here. From Fig. 6.14, one can easily determine that,

$$C_1 \cos\xi_1 = x_1 = y' \sin\alpha - y' \sin(\beta + \gamma) + R_1 \sin\theta \tag{6.1}$$

where $x_1$ is displacement along the X axis at location $C_1$, $y'$ is the displacement along the $Y'$ axis, and so on. The misalignment angles in expression (6.1) are typically of the order of 1ppm. One can justifiably use the small angle approximation, without incurring errors of more than 1ppb. Thus,

$$\begin{aligned} C_1 \cos\xi_1 = x_1 &= y'\alpha - y'(\beta + \gamma) + R_1\theta \\ &= y'(\alpha - \beta) - y'\gamma + R_1\theta \end{aligned} \tag{6.2}$$

Similarly, $C_2 \cos\xi_2 = x_2 = y'(\alpha - \beta) - y'\gamma + R_2\theta$ (6.3)

If $\xi_1$ and $\xi_2$ are small, one can easily obtain the stage yaw error $\theta$ using two measurements $C_1$ and $C_2$, irrespective of what the other stage errors and metrology errors are. Furthermore, $\gamma$ can be eliminated by performing a standard reversal trick. Referring to Fig. 6.15, the artefact is reversed and a third sensor is introduced. This allows for the following additional measurement,

$$C_3 \cos\xi_3 = x_3 = -y'(\alpha - \beta) - y'\gamma - R_3\theta \tag{6.4}$$

Comparing expressions (6.3) and (6.4), it can be noticed that the sign of the $\gamma$ term has been reversed with respect to the other terms, due to the physical reversal of the artefact. Subtracting the two expression eliminates the $\gamma$ term.

As shown in Fig. 6.15, while some of the metrology set-up errors can be eliminated simply by the use of reversal and symmetry, others may pose a more difficult problem. One may notice, for example, that in all of the measurements (6.2) - (6.4), the parameters $\alpha$ and $\beta$ always occur in a particular combination, ($\alpha - \beta$). Some amount of careful thought reveals that no matter what configuration of sensors is used, $\alpha$ and $\beta$ will always occur in the same combination. Hence, it become not just difficult but impossible to distinguish between the two errors.

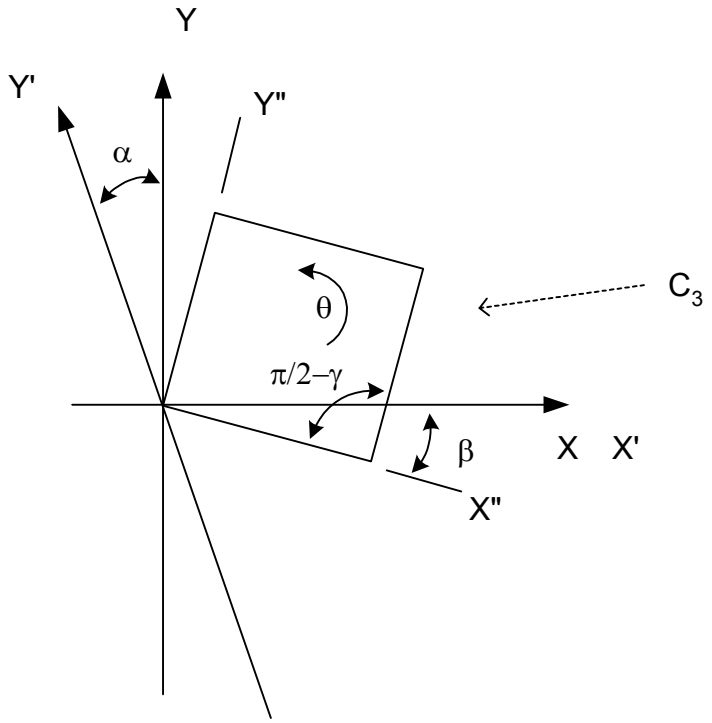


*Fig 6.15*

This brings us to one of the classic problems in metrology – in the error measurement of an XY stage, how does one differentiate between two errors: orthogonality error of the stage and alignment error of the sensor target artefact, without resorting to an explicit measurement of either one. Based on literature searches [88] and discussions with several metrology experts, we have arrived at the conclusion that the two errors remain indistinguishable irrespective of the number and arrangement of sensors used.

The straightness error of the stage and the artefact share the same fate. But in this case, the latter is several orders of magnitude lower than the former, and hence is not as bothersome. On the other hand, a relatively large artefact misalignment error may masquerade as an orthogonality error, thus giving an incorrect assessment of the cross-axis error characteristics of an XY stage. The only suggested remedy to resolve this situation is to explicitly measure the misalignment between the stage and the artefact, which we refer to as target block in the previous discussion. All subsequent measurement should be corrected based on this initial measurement. Another fact that becomes obvious based on this discussion is that good sensor alignment is critical in avoiding cosine errors, and there does not exist an obvious way to cancel these out.

**This page is intentionally left blank**